James Webb Space Telescope observations of the white dwarf cooling sequence of 47 Tucanæ

M. Salaris,[1,2]★ M. Scalco,[3] L. Bedin [3] and S. Cassisi[2,4]

[1]*Astrophysics Research Institute, Liverpool John Moores University, 146 Brownlow Hill, Liverpool L3 5RF, UK*
[2]*Istituto Nazionale di Astrofisica, Osservatorio Astronomico di Abruzzo, via M. Maggini sn, I-64100 Teramo, Italy*
[3]*Istituto Nazionale di Astrofisica, Osservatorio Astronomico di Padova, Vicolo dell'Osservatorio 5, I-35122 Padova, Italy*
[4]*Istituto Nazionale di Fisica Nucleare, Sezione di Pisa, Universitá di Pisa, Largo Pontecorvo 3, I-56127 Pisa, Italy*

ABSTRACT

We present a study of the white dwarf (WD) cooling sequence of the globular cluster 47 Tucanæ (47 Tuc or NGC 104) using deep infrared observations with the *JWST*. By combining these data with ultradeep optical imaging from the *Hubble Space Telescope* (*HST*) taken ∼12 yr earlier, we derived precise proper motions (PMs) and isolated a clean sample of WD cluster members. We estimated the cluster's age by comparing the observed WD cooling sequence luminosity function (LF), derived from *JWST* photometry, with theoretical models, obtaining a value of 11.8 ± 0.5 Gyr, in agreement with main-sequence turn-off ages, and ages determined from the masses and radii of two eclipsing binaries in the cluster. The age determined from the infrared LF is consistent with the optical LF based on the *HST* photometry. However, small discrepancies exist between the shape of the observed and theoretical LFs. To investigate these differences, we tested the cooling times of WD models populating the bright part of the observed cooling sequence against a semi-empirical calibration from the literature, based on bright WDs in 47 Tuc, finding agreement within less than 2σ. A more detailed analysis of dynamical effects and the impact of multiple stellar populations on the WD mass distribution in the observed field will be essential for addressing this discrepancy in future studies.

Key words: white dwarfs – globular clusters: general – globular clusters: individual: NGC 104.

1 INTRODUCTION

The determination of the ages of Galactic globular clusters (GCs) has been a traditional goal of stellar astrophysics, because of its importance in setting a solid lower limit for the age of the Universe, and in providing crucial insights into the process of formation of the Galaxy.

Milky Way-like galaxy haloes are predicted to be built up by the accretion of smaller galaxies plus a contribution from stars and clusters formed *in situ* (see e.g. Abadi, Navarro & Steinmetz 2006; Font et al. 2006; Zolotov et al. 2009), and although the event might destroy completely the accreted dwarf galaxy, but some of its high-density GCs can survive and be added to the *in situ* halo GC population.

The identification of the accreted GCs provides, therefore, additional clues about the past evolution of the Milky Way, and it is indeed a hot topic in current GC research (see e.g. Forbes & Bridges 2010; Massari, Koppelman & Helmi 2019; Massari et al. 2023; Trujillo-Gomez et al. 2023; Belokurov & Kravtsov 2024; Aguado-Agelet et al. 2025). In addition to information about the kinematics (when available) and chemical composition, age also plays an important role in determining whether a GC has originated *in situ* or has been accreted, because of distinctive age–metallicity relationships, as

discussed by e.g. Forbes & Bridges (2010), Leaman, VandenBerg & Mendel (2013), Massari et al. (2019), and Callingham et al. (2022).

For most of the GCs investigated so far, age is determined essentially from their main-sequence (MS) turn-off (TO) luminosity (see e.g. VandenBerg et al. 2013), whilst for just a few clusters it has been possible to compare and confirm the TO age with the age independently determined from their white dwarf (WD) cooling sequence (CS) observed with the *Hubble Space Telescope* (*HST*) and more recently with the *JWST*, namely NGC 6397, M4, and NGC 6752 (see e.g. Hansen et al. 2002, 2007; Bedin et al. 2009, 2023, 2024, 2025).

The well-studied metal-rich GC 47 Tucanæ (47 Tuc, NGC 104) is the fourth GC whose age has been determined from both the TO and its CS, and in addition also from the mass–radius diagram of two eclipsing binaries populating the TO region of the cluster colour–magnitude diagram (CMD; see e.g. VandenBerg et al. 2013; Brogaard et al. 2017; Thompson et al. 2020). Recent age determinations from the TO and eclipsing binaries are consistent, around 12 Gyr, and locate 47 Tuc firmly within the age–metallicity relation of *in situ* GCs.

The cluster age from its CS has delivered so far contradicting results. Using optical *HST* data, Hansen et al. (2013) have obtained 9.9 ± 0.7 Gyr (95 per cent confidence level), which makes 47 Tuc too young for the age–metallicity relation of *in situ* clusters. On the other hand, García-Berro et al. (2014) determined a CS age of around 12 Gyr using a different set of WD models, consistent

with TO and eclipsing binary ages. In between these two results, Campos et al. (2016) found $10.95^{+0.21}_{-0.15}$ and $11.31^{+0.36}_{-0.17}$ Gyr when using the distance modulus and reddening derived from fitting with WD models the bright, age-independent part of the CS, and the distance and reddening obtained by Dotter et al. (2010) from fitting models to the cluster MS, respectively.

For this reason, we have reinvestigated the CS age of 47 Tuc by taking advantage of recent state-of-the-art WD evolutionary models (Salaris et al. 2022) that include among others, convective coupling between envelope and electron degenerate layers, CO phase separation upon crystallization, diffusion of ^{20}Ne in the liquid phase (and also tested the effect of ^{20}Ne distillation upon crystallization), an improved distance from two cluster's eclipsing binaries (Thompson et al. 2020), and new *JWST* observations of the cluster CS.

The plan of the paper is as follows. Section 2 describes the *JWST* data, the reduction process, and the proper motion (PM) selection, whilst Section 3 discusses the artificial star tests. Section 4 presents the WD luminosity function (LF) used in Section 5 to determine the cluster age. A summary and conclusions follow in Section 6.

2 DATA SET AND REDUCTION

The data used in this study were presented in Scalco et al. (2025), to which we refer the reader for a detailed description of the data set and reduction process.

Briefly, the data set originates from *JWST* program GO-2559 (Caiazzo et al. 2021), and observations were conducted using the Near-Infrared Camera (NIRCam; Rieke et al. 2023) over two epochs (∼2022.7 and ∼2023.4) with the *F*150*W*2 filter for the short wavelength channel and the *F*322*W*2 filter for the long wavelength channel. As in Scalco et al. (2025), we rely only on the first epoch's photometry for this study, as it provides deeper and higher quality data.

Data reduction of the images involved a combination of first- and second-pass photometry (see also Nardiello et al. 2022, 2023b; Griggio, Nardiello & Bedin 2023; Libralato et al. 2023, 2024; Nardiello, Griggio & Bedin 2023a; Bedin et al. 2024; Scalco et al. 2024c, for a description of the *JWST* data reduction process), using the software KS2 for the second pass (see Bellini et al. 2017, 2018; Libralato et al. 2018, 2022; Nardiello et al. 2018; Scalco et al. 2021, and references therein for a description of KS2).

The astrometry was anchored to the absolute reference frame provided by *Gaia* Data Release 3 (DR3; Gaia Collaboration 2016, 2023), and the photometry was calibrated to the Vega-magnitude photometric system following the prescription of Bedin et al. (2005).

We selected a sample of well-measured stars by applying quality-based selection criteria using parameters provided by KS2, such as the QFIT (quality of fit), which quantifies the accuracy of the point spread function (PSF) fitting, and RADXS parameters, which measure how closely a source's shape resembles the PSF. The RADXS parameter is particularly useful for distinguishing between point-like (stellar) and extended (non-stellar, e.g. galaxies or blends) sources (see Bedin et al. 2008, 2009). We refer to Scalco et al. (2021) for a comprehensive description of these parameters. In this study, we retained only sources with absolute RADXS values smaller than 0.075 in the *F*150*W*2 filter and smaller than 0.15 in the *F*322*W*2 filter. For the QFIT parameter, we required positive values in both filters, as negative values typically indicate unreliable PSF fitting. In this study, the adopted thresholds are broader than those used in Scalco et al. (2025), which were optimized for MS stars. Because WDs are intrinsically faint, and faint stars tend to have larger photometric uncertainties and degraded shape measurements, stricter cuts would
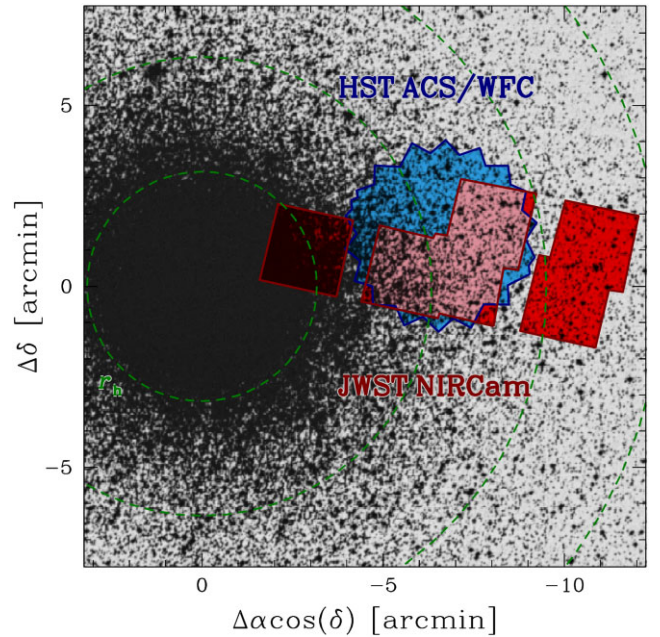
Figure 1. The NIRCam *JWST* field from the first epoch of the GO-2559 programme (red) and the ACS/Wide Field Channel *HST* field from the GO-11677 programme (blue) overlaid on a DSS image of 47 Tuc. The overlap region between the two data sets is highlighted in magenta. Units are in arcmin from the cluster's centre. The green dashed circles represent the half-light radius ($r_h = 3.17$ arcmin; Harris 1996, 2010), with additional circles marking $2\,r_h$, $3\,r_h$, and $4\,r_h$.

unnecessarily exclude a significant number of valid WD candidates. We, therefore, adjusted the selection criteria to strike a balance between data quality and completeness for the WD population, which is the main focus of this work.

In Scalco et al. (2025), PMs were measured using the displacements between the two *JWST* GO-2559 epochs. While the use of *JWST* data provides exceptional depth for PM measurements of red objects (invisible in the optical), the short temporal baseline between the two *JWST* epochs (∼7 months) limits the accuracy of PM estimates for fainter stars, such as the WDs targeted in this study. This baseline was adequate for the analysis in Scalco et al. (2025), but for this work, a longer temporal baseline is essential for an accurate measure of the PMs of faint – bluer – stars and to disentangle them from objects in the Small Magellanic Cloud (SMC).

To address this limitation, we include *HST* images from program GO-11677 (Richer 2009), taken between 2010 January 15 and 2010 October 1 (epoch ∼2010.4). These *HST* images partially overlap with the *JWST* GO-2559 field of view (FOV) and provide a significantly longer temporal baseline, enabling more precise PM measurements. They were collected by the Advanced Camera for Surveys (ACS) with the *F*606*W* and *F*814*W* filters. The reduction of the *HST* images was performed following the same first- and second-pass photometry procedures applied to the *JWST* data (see Scalco et al. 2021, for additional details on *HST* data reduction). Fig. 1 shows the positions of our *JWST* and *HST* data sets within the FOV, overlaid on a Digital Sky Survey (DSS) image of 47 Tuc.[1]

PMs were calculated as the displacements of stars common to both the *JWST* and *HST* data sets, divided by the temporal baseline (∼12 yr). The resulting PMs for our selected sample of well-

[1] https://archive.eso.org/dss/dss

measured stars with detectable PMs are shown in Fig. 2. Panel (a) shows the vector-point diagram (VPD), while panel (b) shows the m_{F150W2} versus $m_{F150W2} - m_{F322W2}$ CMD, focused on the low MS, the SMC MS, and the cluster CS. In the VPD, two distinct groups of stars are evident: the cluster members, centred at (0, 0), and the SMC stars, located around (5, -0.5). The distribution of points in this study is significantly narrower than that in Scalco et al. (2025, see fig. 3), owing to the larger temporal baseline used here.

Panel (c) displays the one-dimensional PM (μ_R), obtained by combining the PM components in quadrature, plotted against m_{F150W2}. The separation between cluster members and SMC stars is particularly evident along the MS and remains clear for stars on the WD CS. Most 47 Tuc cluster members are concentrated below $\mu_R < 2.5$ mas yr^{-1}, whereas SMC stars cluster around $\mu_R \sim 5$. A PM-based selection criterion, indicated by a vertical red line, was defined to separate cluster members (located on the left side of the line) from SMC objects (on the right side of the line).

Panel (d) displays the VPD for stars that passed the PM selection, while panel (e) presents the corresponding CMD, where the WD CS of the cluster is visible clearly. Finally, panels (f) and (g) show the VPD and CMD, respectively, for stars that did not satisfy the PM selection criteria. From panel (f), it is evident that a small number of stars remain near the cluster's PM locus after applying the selection criterion, suggesting a residual level of contamination in the cluster sample. We estimated the contamination rate using artificial stars (see Section 3) by calculating the fraction of artificial stars rejected solely based on their PMs, relative to the total number of artificial stars. This analysis indicates an estimated contamination rate of ~8 per cent.

Fig. A1 in Appendix A presents a set of CMDs of the WD CS of 47 Tuc, using various combinations of the four *HST* and *JWST* filters employed in this study. The CMDs include all well-measured sources that passed the PM selection described in Fig. 2.

3 ARTIFICIAL STARS

We performed artificial star tests to evaluate the completeness and estimate the photometric errors in our sample. A total of 10^5 artificial stars were generated, uniformly distributed across the overlapping FOV between the *JWST* and *HST* data sets. The $F150W2$ magnitudes of these artificial stars were uniformly sampled within the range $22 < m_{F150W2} < 30.5$. The corresponding magnitudes in the $F322W2$, $F606W$, and $F814W$ filters were assigned based on fiducial lines manually defined on the m_{F150W2} versus $m_{F150W2} - m_{F322W2}$, m_{F150W2} versus $m_{F606W2} - m_{F150W2}$, and m_{F150W2} versus $m_{F814W2} - m_{F150W2}$ CMD, respectively. These fiducial lines trace the WD CS, extending to the apparent faint end of the sources, and are extrapolated to even fainter magnitudes.

The artificial stars were generated, detected, and measured using KS2, following the same procedures applied to the real stars. Artificial PMs were generated by separately processing the artificial stars for the *JWST* and *HST* data sets and evaluating their displacements between the two epochs.[2]

We followed the methodology described in Bedin et al. (2009, section 2.3) to correct for systematic errors between input and output magnitudes in both real and artificial sources. We found these

corrections negligible (<0.1 mag) for the *JWST* data down to the faintest magnitudes studied; therefore, we applied them only to the *HST* photometry.

An artificial star is considered successfully recovered if the difference between its input and output positions is less than 1 pixel, the difference in magnitudes is within 0.75 (equivalent to ~2.5 log 2) in both filters, and if it passes the same selection criteria applied to real stars. The completeness is then calculated as the ratio between the recovered and the injected artificial stars as a function of the magnitude.

Fig. 3 shows the m_{F150W2} versus $m_{F150W2} - m_{F322W2}$ CMD for the real stars (points in panel a) and the recovered artificial stars (points in panel b), with the injected artificial stars represented in magenta in both panels. To isolate the WDs, we manually defined two fiducial lines (shown in green) that enclose the WD CS in both panels. These fiducial lines will be used in the following to define the sample of WDs for the LF study.

We employed the artificial stars to estimate photometric errors as a function of magnitude for each of the four filters. To do this, the recovered artificial stars were divided into 0.5-mag bins for each filter. Within each bin, we computed the 2.5σ-clipped median of the distribution of differences between the injected and recovered magnitudes. The final σ value from the clipping process was adopted as our estimate of the photometric error.

4 LUMINOSITY FUNCTION

In this section, we present the LF of the WD CS in 47 Tuc, based on *JWST* data. The analysis is shown in Fig. 4. To evaluate the LF, we initially excluded the selection based on the KS2 photometric quality parameters and considered a sample of stars selected only using the PM criteria shown in Fig. 2.

Panel (a) shows the m_{F150W2} versus $m_{F150W2} - m_{F322W2}$ CMD for these sources, where the green lines, previously introduced in Fig. 3, define the WD selection region. Objects within this region are represented in black, while all other sources are shown in grey.

Panel (b) presents the observed LF of the selected WDs as a black histogram. The completeness corresponding to the selected sample, as a function of m_{F150W2} magnitude, is shown as a solid line, with its corresponding values shown on the secondary axis at the top of the panel. The dashed line represents c_g, the completeness values restricted to the darker usable areas for detecting faint sources (see Bedin et al. 2008, 2009, for further details). The completeness-corrected LF is displayed as a blue histogram. Error bars indicate uncertainties: for the observed LF, they correspond to Poisson errors, while for the completeness-corrected LF, they result from uncertainty propagation.

We then repeated the analysis by adding a selection based on the KS2 photometric quality parameters. The results are displayed in panels (c) and (d), together with the corresponding completeness.

The completeness-corrected LF in panel (b) is noisier compared to the one in panel (d) due to higher contamination from poorly measured or non-member sources. On the other hand, the LF presented in panel (d) is cleaner and more reliable but suffers from significantly lower completeness near the peak ($m_{F150W2} \sim 27.5$), reaching values as low as 5 per cent, below the thresholds typically considered reliable.

Panel (e) shows the comparison between the two completeness-corrected LFs: the one obtained in panel (b) is shown in red, while the one from panel (d) is shown in blue. The red LF and its errors have been normalized to align the peaks of both LFs.

---

[2]Spurious positional offsets due to noise, especially in faint stars, can affect PM measurements and membership selection. Since artificial stars are generated with identical positions in both epochs, any observed displacement is solely ascribed to noise. This approach allows us to quantify this effect and include it in the completeness evaluation.
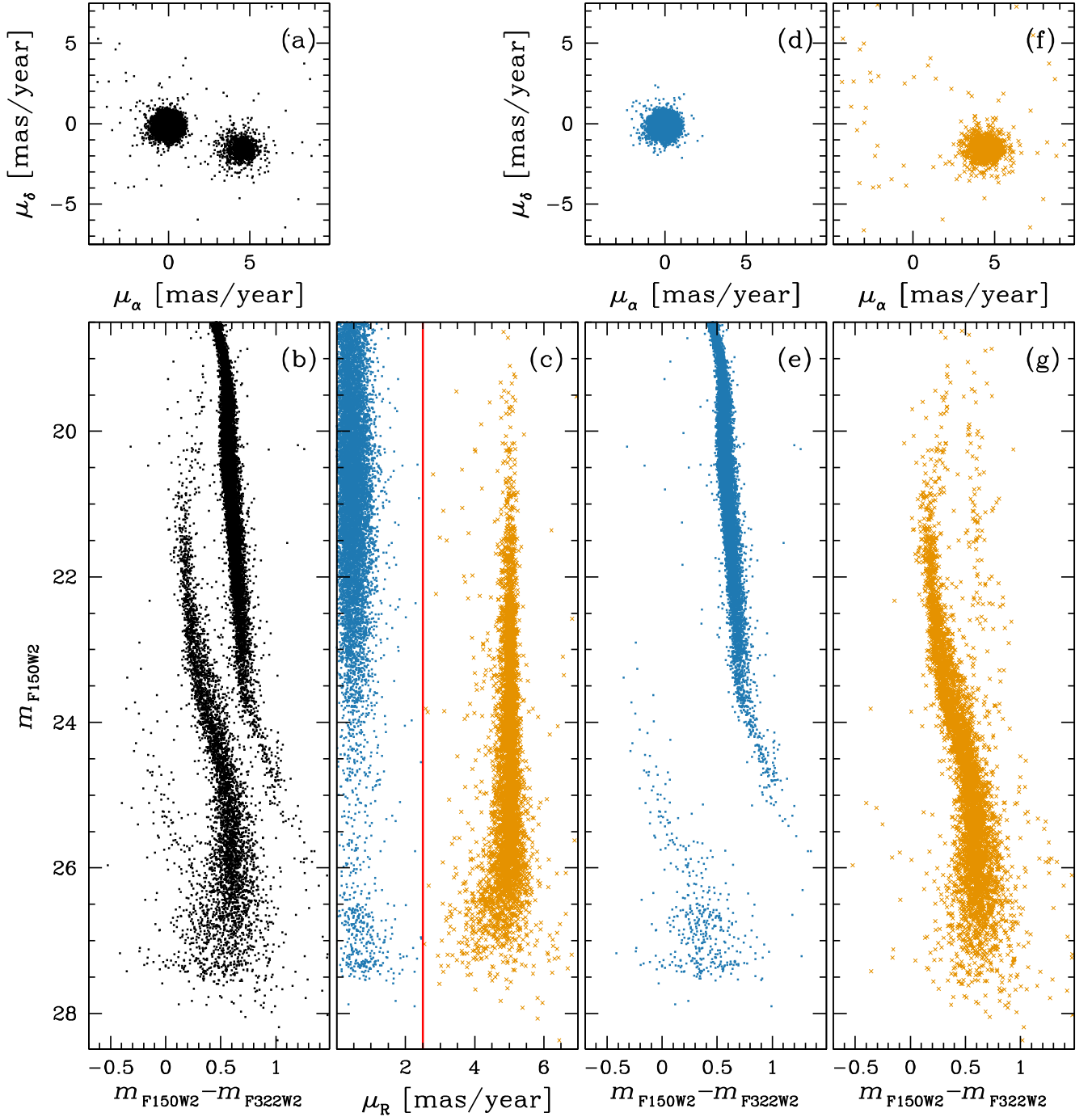
Figure 2. Custer membership selection based on PMs. The figure displays only well-measured stars that meet the KS2 quality selection criteria and have detectable PMs. (a) VPD. (b) m_{F150W2} versus $m_{F150W2} - m_{F322W2}$ CMD, focused on the low MS, the SMC MS, and the WD CS. (c) m_{F150W2} magnitude versus the one-dimensional PM (μ_R). The red line separates cluster members from field stars. (d)–(e) VPD and m_{F150W2} versus $m_{F150W2} - m_{F322W2}$ CMD for stars that passed the PM selection. (f)–(g) The same diagrams for stars that did not pass the PM selection. In panels (c) through (g), sources that passed the PM selection are represented by blue dots, while the others are depicted as orange crosses.

As shown, the two LFs are completely consistent with each other. While the completeness for the blue LF is very low below the LF peak ($m_{F150W2} > 27.5$), with values approaching 0 (see panel d), the completeness for the red LF in this region remains acceptable, around 20 per cent (see panel b). None the less, the drop below the peak is also observed in the red LF, confirming that the drop is real and not an artefact of the stricter selection criteria. The consistency

between the two LFs supports the validity of the blue LF, even at lower completeness levels.

For the age determination discussed in the next section, we will focus exclusively on the blue LF shown in panel (e), as it is the most reliable due to its higher precision and reduced contamination.

For comparison, and to use as a consistency check of the ages derived from the *JWST* LF, we also derived the WD LF from the
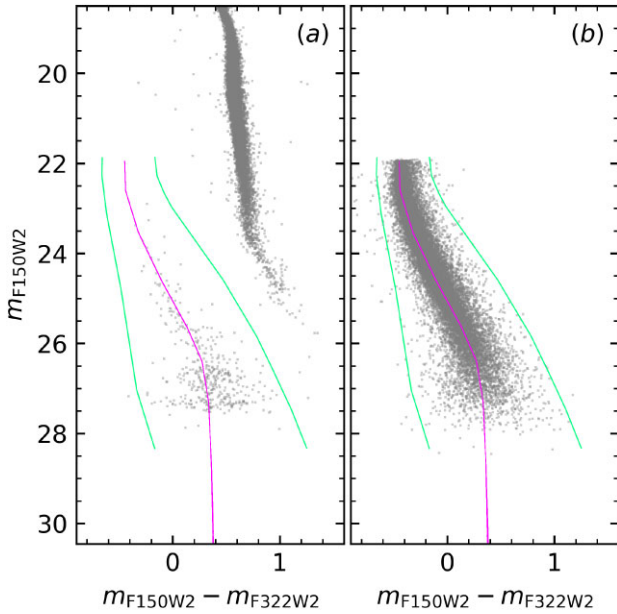
Figure 3. (a) m_{F150W2} versus $m_{F150W2} - m_{F322W2}$ CMD for the real stars. (b) Same as panel (a) but for the recovered artificial stars. In both panels, magenta points distributed along a line that crosses the observed CS represent the injected artificial stars. The two (green) fiducial lines are used to isolate the stars along the WD CS.

HST photometry in our data set. We selected the same sample of stars used to estimate the blue LF in panel (e), applying both the KS2 photometric quality parameters and the PM-based membership selection. However, in this case, we defined the WD CS in the m_{F606W} versus $m_{F606W} - m_{F814W}$ CMD using two fiducial lines, following the approach illustrated in Fig. 3. The completeness-corrected LF is presented in panel (f) of Fig. 4. As seen in the figure, the overall shape of this LF closely resembles that of the *JWST*-derived LF.

The infrared LF used for the WD age determination and the optical counterpart from *HST* data are publicly available on our website[3] and are tabulated in Tables B1 and B2 in Appendix B.

5 THE AGE OF 47 TUC FROM ITS WD COOLING SEQUENCE

To determine the age of 47 Tuc from its CS, we have taken advantage of the BASTI-IAC hydrogen-atmosphere WD models[4] and isochrones (see Salaris et al. 2022, for a detailed description of the models) calculated with the Cassisi et al. (2007) electron degeneracy opacities, for a progenitor metallicity corresponding to [Fe/H] = −0.7,[5] consistent with [Fe/H] = −0.66 ± 0.04 derived by Gratton et al. (2003), [Fe/H] = −0.67 ± 0.05 obtained by Carretta et al. (2004), [Fe/H] = −0.768 ± 0.016 ± 0.031 (random and systematic errors) measured by Carretta et al. (2009), and −0.70 ± 0.01 ± 0.04 (random and systematic errors) determined by Koch & McWilliam (2008) from high-resolution spectroscopy. In the calculation of the isochrones we have employed progenitor

---

[3]https://web.oapd.inaf.it/bedin/files/PAPERs_eMATERIALs/JWST/Paper_47Tuc_WDCS/

[4]See Davis et al. (2009) for the apparent dearth of helium-atmosphere WDs in GCs. In Appendix C, we show the effect of including helium-atmosphere objects in our analysis.

[5]The WD models can be found at http://basti-iac.oa-abruzzo.inaf.it/.

lifetimes from the BASTI-IAC α-enhanced ([α/Fe] = 0.4) models by Pietrinferni et al. (2021), and the WD initial–final mass relation by Cummings et al. (2018). The WD models include, among others, the effect of convective coupling between the envelope and electron degenerate layers, latent heat release and CO phase separation upon crystallization, plus ^{22}Ne diffusion in the liquid phase (see Salaris et al. 2022, for details). At this metallicity the diffusion of ^{22}Ne increases the cooling time by at most 200–300 Myr for the faintest objects.

We have also calculated with the same code of the WD computations some test models that in addition include ^{22}Ne distillation during crystallization (see Blouin, Daligault & Saumon 2021; Bédard, Blouin & Cheng 2024; Salaris et al. 2024), and found that at the cluster's relatively low metallicity this process has a negligible impact on the energy budget and cooling times.

Fig. 5 displays the CMD of the CS and the very low MS stars in NGC 6397 (from Bedin et al. 2024) and 47 Tuc, this latter CMD shifted in magnitude and colour to the same distance and reddening of NGC 6397. Here and in the rest of this work, we have employed as reference values for the distance modulus of 47 Tuc $(m − M)_0 = 13.29$, taken from the analysis of two cluster's eclipsing binaries by Thompson et al. (2020),[6] and for the reddening $E(B − V) = 0.024$ (Gratton et al. 2003), using the extinction ratios A_λ/A_V we employed in Bedin et al. (2024), whilst for NGC 6397 we have used $(m − M)_0 = 11.96$ and $E(B − V) = 0.18$ (see Bedin et al. 2024).

As found in optical *HST* filters by Richer et al. (2013) and Hansen et al. (2013), also in the infrared the overall morphology of 47 Tuc CS is consistent with that of the much more metal-poor GC NGC 6397 ([Fe/H] $\sim −2.0$). Whilst the lower MS of 47 Tuc is redder because of its higher metallicity, the two CSs overlap nicely. The termination of the shifted 47 Tuc CS is however brighter than the NGC 6397 counterpart, like in the optical, suggesting an age younger than the $\sim$13 Gyr found by Bedin et al. (2024) for NGC 6397 using the same models (for both WDs and their progenitors) employed in this analysis.

Fig. 6 shows a first qualitative comparison between the m_{F150W2} versus $m_{F150W2} - m_{F322W2}$ synthetic CMD generated from a 12 Gyr WD isochrone, and the observed CS. We use the CS in panel (c) of Fig. 4, consistent with the LF of panel (d) employed in the rest of this analysis, as discussed in the previous section.

The synthetic CS has been calculated by first drawing progenitor masses along the isochrone using a power-law mass function (MF) $dN/dM \propto M^\alpha$, with $\alpha = -2.35$; the corresponding WD and its $F150W2$ and $F322W2$ magnitudes were then determined by quadratic interpolation along the isochrone. We then added our adopted reference distance modulus and extinction values to these magnitudes and perturbed them randomly using Gaussian photometric errors inferred from the artificial star tests. We finally randomly chose whether a synthetic WD is observable using our determined completeness fraction as a function of the observed magnitudes.

The CMD of the synthetic objects that pass the completeness test (their number is similar to that of the observed sample) nicely overlaps the area covered by the observed WDs.
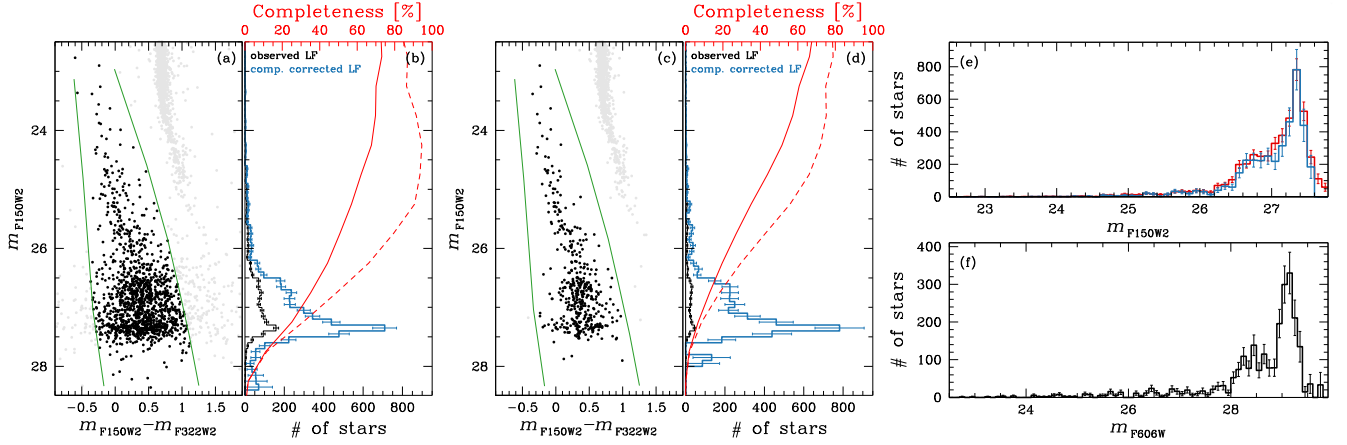
For a more quantitative determination of 47 Tuc age from its CS, we compared the completeness-corrected observed WD LF with its theoretical counterparts. The theoretical LFs have been obtained from the calculation of synthetic CMDs, as described above, to

---

[6]Parallax and kinematic distance determinations from *Gaia* DR3 are consistent with the eclipsing binary distance (Baumgardt & Vasiliev 2021).
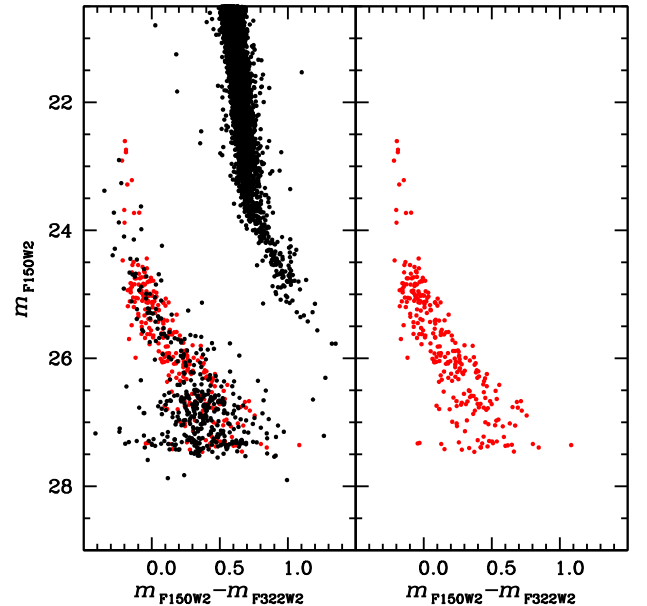
Figure 4. LF of the CS of 47 Tuc. (a) m_{F150W2} versus $m_{F150W2} - m_{F322W2}$ CMD of stars that pass only the PMs selection. The green line defines the region used to select WDs for the evaluation of the LF. The selected WDs are shown in black, while all other sources are shown in grey. (b) Observed (black) and completeness-corrected (blue) LF of the WDs selected in panel (a), with the corresponding errors shown as error bars. The standard completeness and c_g as a function of the m_{F150W2} magnitude are represented as solid and dashed red lines, respectively, with the corresponding axis shown at the top of the panel. (c)–(d) Same as panels (a) and (b), but for stars passing both the PMs and the selections based on KS2 photometric quality parameters. (e) Comparison of the LFs derived from the two samples: the LF for stars that pass only the PMs selection is shown in red, while the LF for stars that pass both the PMs and photometric selections is shown in blue. Note that the red LF and its errors have been normalized to align the peaks of both LFs. (f) LF of 47 Tuc derived using optical *HST* photometry.
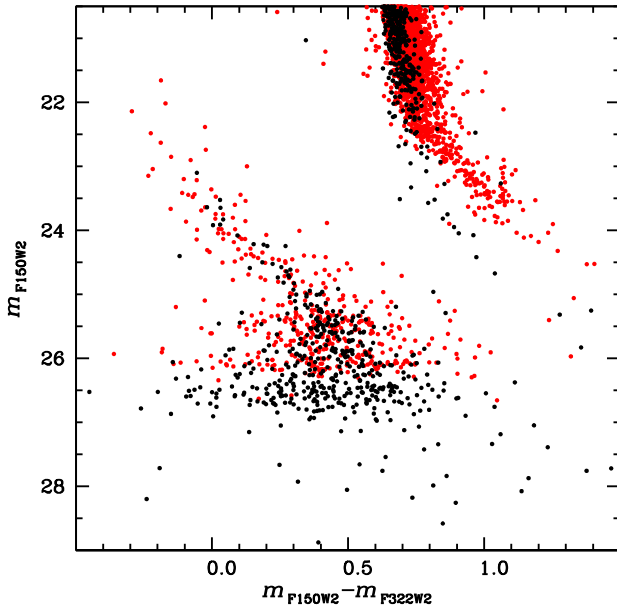
Figure 5. CMD of NGC 6397 CS (black dots – from Bedin et al. 2024) compared to the 47 Tuc CS (red dots – the same sequence of Fig. 6) shifted in magnitude and colour to the same distance and reddening of NGC 6397.

Figure 6. The right panel displays a synthetic CMD of a 12-Gyr-old WD population with [Fe/H] = −0.7 progenitors, photometric errors, and completeness fractions as those derived from the artificial star tests, shifted to 47 Tuc distance modulus and reddening (see text for details). The left panel shows the same synthetic WDs (red dots) together with the observed CMD of 47 Tuc CS and very low MS (black dots).

include the effect of the photometric errors. In the comparison with completeness-corrected LF, we included the entire sample of synthetic objects, not just those that passed the completeness test.

Fig. 7 displays the observed LF together with two theoretical LFs for ages equal to 11.5 and 11.9 Gyr, normalized to match the observed number of stars in the well-populated magnitude range $m_{F150W2} = 26.6$–26.9, where the star counts are still unaffected by the choice of the exact value of the cluster age. The theoretical LFs display a peak covering the three bins centred at m_{F150W2} between 27.25 and 27.45, and a sharp decrease at the same magnitudes as their observed counterpart. Ages outside this range produce LFs with the

peak either brighter (age too young) or fainter (age too old) than the observed one.

We can also notice that the shape of the observed LF is not matched in its details by theory. In particular, at magnitudes brighter than the range used for the normalization, the predicted number counts are larger than the observations, especially in the range $m_{F150W2} \sim 25.85$–26.45. To investigate this issue further, we show in Fig. 8 the distribution of WD and progenitor masses along the isochrones employed to calculate the LFs in Fig. 7. Down to
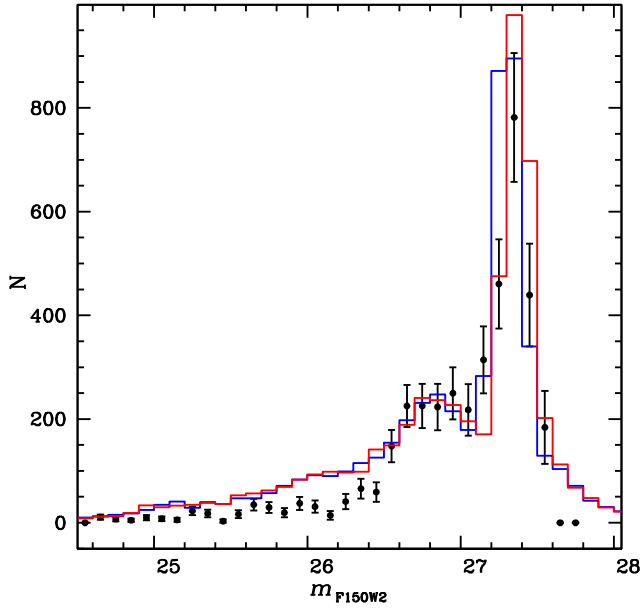
Figure 7. Comparison of the observed WD LF (filled circles with error bars) and two theoretical LFs calculated for ages equal to 11.5 Gyr (blue histogram) and 11.9 Gyr (red histogram; see text for details).
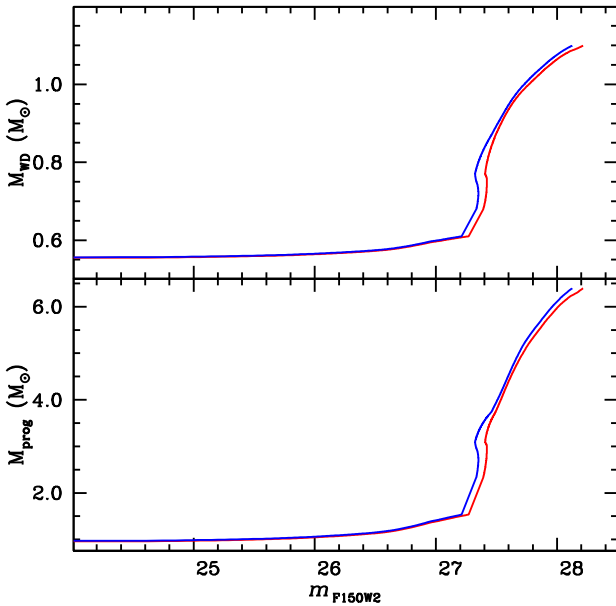
Figure 8. Values of the WD mass (M_{WD}) and the corresponding progenitor mass (M_{prog}) as a function of m_{F150W2}, along the 11.5 Gyr (blue line) and 11.9 Gyr (red line) WD isochrones shifted to account for the cluster extinction and distance modulus.

$m_{F150W2} \sim 26.2$–26.5, the isochrones are populated by WDs with essentially constant mass; indeed, in the range between $m_{F150W2} \sim 25.0$ and $m_{F150W2} \sim 26.4$ – corresponding to effective temperatures between $\sim 11\,000$ and ~ 5500 K – the value of the WD mass M_{WD} ranges from 0.557–0.558 to 0.570–0.572 $M_\odot$, an almost negligible increase due to a combination of the short cooling times (compared to the cluster age) at these luminosities and the almost constant value of the final WD mass for progenitors with initial masses up to $\sim 2\,M_\odot$ (see Cummings et al. 2018).
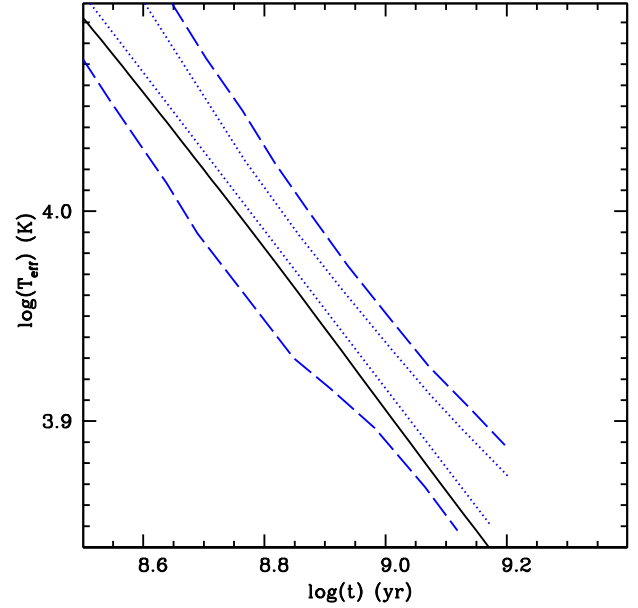
Figure 9. Semi-empirical CS (T_{eff} versus age) for the bright WDs in 47 Tuc (from Goldsbury et al. 2012) compared to a theoretical 0.56 $M_\odot$ counterpart (solid line) from our adopted WD calculations. The dotted lines enclose the 1σ error range of the semi-empirical sequence, whilst the dashed lines mark the 2σ error interval (see text for details).

It is also important to note that at m_{F150W2} fainter than ~ 27.2 mag, the mass of the WD (and progenitors) displays a very steep increase with increasing m_{F150W2}. In the magnitude range of the observed narrow peak of the LF, the isochrones are populated by objects with masses between ~ 0.6 and ~ 0.95–1.0 $M_\odot$, encompassing almost the whole mass spectrum of CO WDs. This steep increase of the WD mass over a narrow magnitude increase near the faint end of the isochrone translates to a pile-up of objects in the LF, and produces the observed peak, which gets fainter with increasing age because of the increased cooling times of the WDs.

The property that the bright part of a GC CS is populated by objects with virtually constant mass was exploited by Goldsbury et al. (2012) to determine a semi-empirical CS for the bright WDs in 47 Tuc, in the temperature range between $\sim 40\,000$ and ~ 7000 K. After measuring the T_{eff} of a large sample of WDs, and assuming that the rate at which stars enter the CS is constant, Goldsbury et al. (2012) employed stellar evolution models for the WD progenitors to determine the rate at which stars leave the MS, which must be the same as the rate at which objects enter the CS.[7] The result of their analysis was a semi-empirical relation between T_{eff} and cooling times for the constant mass objects populating the bright WDs in 47 Tuc.

Fig. 9 compares this semi-empirical cooling law with results from BASTI-IAC WD calculations for a representative 0.56 $M_\odot$ WD model. The highest temperature considered in the comparison corresponds to $m_{F150W2} \sim 25$, while the lowest temperature is at the cool limit of the semi-empirical calibration, which corresponds to $m_{F150W2} \sim 26$. The figure shows that in this magnitude range, the models are consistent

---

[7]The authors discounted the possibility that dynamical relaxation of the WDs could make this assumption invalid, because the relaxation time evaluated for their field is too long compared to the time elapsed between the progenitors of their faintest observed WDs leaving the MS and their WD progeny reaching their observed luminosity.
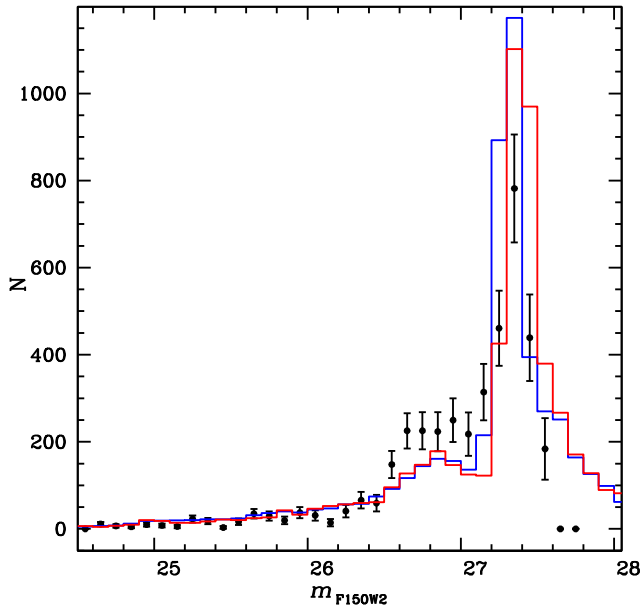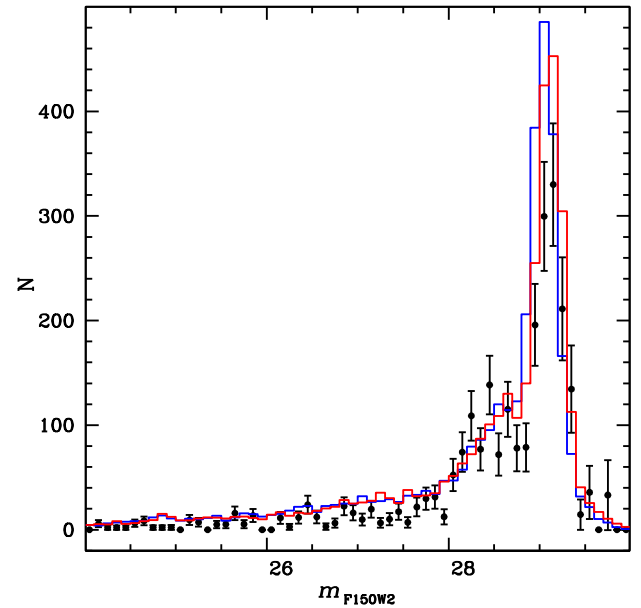
Figure 10. As Fig. 7 but the theoretical LFs are calculated with a top-heavy MF for the WD progenitors (see text for details).

Figure 11. As Fig. 7 but the observed and theoretical LFs are in the *HST*/ACS *F*606*W* filter (see text for details).

with the semi-empirical calibration within less than 2σ, hence it is unlikely that the overpredicted star counts in the magnitude range between 25.85 and 26.45 are due to an overestimate of the cooling times by the WD models.

The main reason for this mismatch and the general inability of the theoretical LFs to match the exact star counts across the full magnitude range is likely because the WD mass distribution along the CS depends in a complex way on the progenitors' initial MF, and dynamical evolutionary effects (escape from the cluster of WD progenitors, mass segregation that has caused a spatial redistribution of the WDs and their progenitors) that have affected both the progenitors' and the WD mass distribution in the observed field (see e.g. Richer et al. 2013). We will go back to this point at the end of the section.

At this stage, we show in Fig. 10 the effect of varying only the progenitors' MF exponent when comparing observed and theoretical LFs; changing this exponent does alter the mass WD mass distribution along the CS. The 11.5 and 11.9 Gyr LFs shown in the figure have been calculated using a top-heavy progenitor's MF with an exponent equal to -1.3, without altering their normalization. This modification of the progenitor's MF increases the number of more massive WDs compared to the less massive ones, and the bright part of the observed LF is now reasonably well matched by theory, although there is an obvious mismatch at fainter magnitudes. A single exponential power law for the progenitors' MF clearly is not a good approximation; however, for our purposes, the important point is that the magnitude range of the peak of the LF – the age indicator – is a solid prediction.

If we account for conservative errors of ± 0.05 mag on the eclipsing binary distance (considering the spread of the individual components' distances determined with the two methods discussed in Thompson et al. 2020), ± 0.1 dex on [Fe/H], and $E(B-V)$ ranging from the reference $E(B-V) = 0.024$ value taken from Gratton et al. (2003) to the more standard $E(B-V) = 0.04$ (see e.g. Koch & McWilliam 2008), the total age range compatible with the position of the peak of the observed LF ranges between 11.3 and 12.3 Gyr. The contributions of the uncertainties on the reddening and [Fe/H] are

negligible compared to the effect of the uncertainty on the distance modulus.

As a further step in our analysis, we have checked the consistency between the cluster age determined from *JWST* and *HST* observations. Fig. 11 compares the completeness-corrected optical LF with theoretical LFs for 11.5 and 11.9 Gyr (as in Fig. 7), calculated with the same progenitors' MF, the reference distance modulus, and reddening employed in Fig. 7, extinction A_{F606W} computed following Bedin et al. (2005), and photometric errors obtained from the artificial star analysis of the *HST* observations. The theoretical LFs have been rescaled to match the observed number of stars between $m_{F606W} = 28.05$ and 28.65, corresponding approximately to the same magnitude range of the *JWST* LF normalization. As we found and discussed for the infrared data, there is on average an excess of objects at magnitudes brighter than the normalization interval, and more in general the theoretical LFs do not match the detailed shape of the observed counterpart. The position of the peak in the observed LF sensitive to age is nicely bounded by the two theoretical LFs, as in the case of the *JWST* data, confirming the consistency between the ages obtained from infrared and optical observations of the CS.

5.1 The impact of the cluster multiple populations

It is well established that 47 Tuc stars display a range of initial helium abundances. Indeed, analyses of the cluster CMD (MS, subgiant branch, red giant branch, and horizontal branch) by several groups (see e.g. Anderson et al. 2009; Di Criscienzo et al. 2010; Salaris, Cassisi & Pietrinferni 2016; Milone et al. 2018) have disclosed a range of initial He mass fractions $\Delta Y = 0.02$–0.03. This spread of initial He abundance is a manifestation of the presence of multiple, roughly coeval stellar populations in the cluster, a common occurrence in massive star clusters like the Galactic GCs (see e.g. Gratton, Carretta & Bragaglia 2012; Bastian & Lardo 2018; Cassisi & Salaris 2020; Milone & Marino 2022, and references therein).

In our adopted progenitor models a metallicity [Fe/H] $= -0.7$ corresponds to a standard $Y = 0.255$ (see Pietrinferni et al. 2021,

for details), hence the initial helium spread in the cluster can be taken into account by considering models with Y between 0.255 and 0.275–0.285. We have verified using models in the BASTI-IAC data base (Pietrinferni et al. 2021) and by computing appropriate test calculations with the BASTI-IAC code, which for $\Delta Y = 0.03$ the variation of the initial mass of TO stars (at fixed age) in [Fe/H] $= -0.7$ α-enhanced old isochrone with ages between 10 and 12 Gyr equals just ~ 0.03 $M_\odot$ (the mass is reduced when the initial helium increases). In the assumption that the WD initial–final mass relation (we remind the reader that we employ the semi-empirical relation derived by Cummings et al. 2018) is not affected by this small variation of initial helium, the mass of the objects evolving along the bright part of the corresponding WD isochrone is essentially unchanged compared to the standard $Y = 0.255$ case. As for the more massive WDs in the region of the peak of the LF, the variation of their progenitor lifetime due to a small non-zero ΔY is negligible compared to the cooling age at those magnitudes. As a result, the presence of a small Y spread among 47 Tuc stars should not have affected appreciably our age determination described in this section.

The presence of multiple populations in the cluster, however, might have an impact on the detailed shape of the WD LF. Multiple stellar populations, potentially characterized by different initial stellar MFs (e.g. Scalco et al. 2024a), tend to exhibit distinct spatial distributions, as observed in other massive GCs like ω Centauri (e.g. Bellini et al. 2009; Scalco, Bedin & Vesperini 2024b). These spatial variations reflect the different kinematical properties of the medium from which the various stellar populations formed (e.g. Bellini et al. 2015), and they are an additional reason why a simple power-law description of the WD progenitor MF used in the calculation of the theoretical WD LFs is very likely not appropriate to match the exact shape of the observed LFs.

6 SUMMARY AND CONCLUSIONS

In this work, we studied the WD CS of the GC 47 Tuc. We employed recent deep infrared observations from *JWST* (GO-2559; Caiazzo et al. 2021), obtained in ~ 2022.7 with NIRCam's ultrawide filters (see Scalco et al. 2025, for a complete description of the data set), and ultradeep optical imaging from *HST* (GO-11677; Richer 2009) of an overlapping field, taken with ACS in ~ 2010.4.

Thanks to the ~ 12-yr time baseline, we measured precise PMs, which allowed us to isolate a clean sample of cluster members. This selection effectively separated cluster WDs from foreground Galactic field stars, background SMC members, and unresolved distant galaxies.

Using this cleaned WD sample, we derived the LF of the WD CS in both *JWST* infrared and *HST* optical filters. The two LFs exhibit a similar shape, peaking at $m_{F150W2} \sim 27.5$ ($m_{F606W} \sim 29.1$).

We have then determined the age of the cluster by employing the *JWST* CS LF, and obtained a value of 11.8 ± 0.5 Gyr, where the error includes the uncertainty due to matching the magnitude range of the peak of the LF and the uncertainty on the eclipsing binary distance modulus (Thompson et al. 2020) assumed for the cluster (the uncertainties on the cluster metallicity and reddening give a negligible contribution). In the process, we have tested the cooling times of the WD model (with a mass of 0.56 $M_\odot$) populating the bright part of the cluster CS by comparison with the semi-empirical calibration by Goldsbury et al. (2012), based on observations of the bright WDs 47 Tuc. We found that the model agrees with this calibration within less than 2σ.

We have also found that the age derived from the infrared CS LF is consistent with the optical LF obtained from the *HST* observations.

When comparing with the previous 47 Tuc CS analyses by Hansen et al. (2013) and García-Berro et al. (2014) that made use of optical *HST* data, our age estimate is higher than the 9.9 ± 0.7 Gyr (95 per cent confidence level) determined by Hansen et al. (2013) using different cooling models (Hansen 1999), despite a distance modulus that is almost the same (larger by just 0.03 mag) as the one employed in our analysis. Our result is instead consistent with García-Berro et al. (2014) who employed the Renedo et al. (2010) WD models and determined 12.5 $\pm$ 0.5 and 12.5 $\pm$ 1.0, depending on the method used (there is no information in the paper about the distance modulus).

Regarding the study by Campos et al. (2016), who made use of Romero, Campos & Kepler (2015) WD models, our age estimate is consistent with their age obtained using the distance $((m - M)_0 = 13.26$, just 0.03 mag shorter than our adopted eclipsing binary distance) and reddening ($E(B - V) = 0.023$) derived from fitting models to the MS (Dotter et al. 2010). When fitting the bright part of the CS to models, the higher derived reddening ($E(B - V) = 0.045$) and distance modulus (0.02 mag longer) combine to decrease the age estimate and explain the difference of the two different ages estimated by Campos et al. (2016).

Finally, our cluster age determined from the CS in the infrared confirms 47 Tuc age derived from the cluster MS TO (11.75 ± 0.25 Gyr as determined by VandenBerg et al. 2013) and by the joint analysis of the TO and the mass–radius diagram of two eclipsing binaries in the cluster (12.0 $\pm$ 0.5 Gyr as determined by Thompson et al. 2020), and the location of 47 Tuc within the body of the age–metallicity relation for *in situ* GCs (see e.g. Leaman et al. 2013).

DATA AVAILABILITY

The WD models employed in this work are available at http://basti-ia c.oa-abruzzo.inaf.it/. The LFs are available at https://web.oapd.inaf.it /bedin/files/PAPERs_eMATERIALs/JWST/Paper_47Tuc_WDCS/.

REFERENCES

Abadi M. G., Navarro J. F., Steinmetz M., 2006, MNRAS, 365, 747

Aguado-Agelet F. et al., 2025, preprint (arXiv:2502.20436)

Anderson J., Piotto G., King I. R., Bedin L. R., Guhathakurta P., 2009, ApJ, 697, L58

Bastian N., Lardo C., 2018, ARA&A, 56, 83

Baumgardt H., Vasiliev E., 2021, MNRAS, 505, 5957

Bédard A., Blouin S., Cheng S., 2024, Nature, 627, 286

Bedin L. R., Cassisi S., Castelli F., Piotto G., Anderson J., Salaris M., Momany Y., Pietrinferni A., 2005, MNRAS, 357, 1038

Bedin L. R., King I. R., Anderson J., Piotto G., Salaris M., Cassisi S., Serenelli A., 2008, ApJ, 678, 1279

Bedin L. R., Salaris M., Piotto G., Anderson J., King I. R., Cassisi S., 2009, ApJ, 697, 965

Bedin L. R. et al., 2023, MNRAS, 518, 3722

Bedin L. R. et al., 2024, Astron. Nachr., 345, e20240039

Bedin L. R. et al., 2025, Astron. Nachr., 346, e20240125

Bellini A., Piotto G., Bedin L. R., King I. R., Anderson J., Milone A. P., Momany Y., 2009, A&A, 507, 1393

Bellini A. et al., 2015, ApJ, 810, L13

Bellini A., Anderson J., Bedin L. R., King I. R., van der Marel R. P., Piotto G., Cool A., 2017, ApJ, 842, 6

Bellini A. et al., 2018, ApJ, 853, 86

Belokurov V., Kravtsov A., 2024, MNRAS, 528, 3198

Blouin S., Daligault J., Saumon D., 2021, ApJ, 911, L5

Brogaard K., VandenBerg D. A., Bedin L. R., Milone A. P., Thygesen A., Grundahl F., 2017, MNRAS, 468, 645

Caiazzo I. et al., 2021, Brown Dwarfs, White Dwarfs and Planetary Disks in an Ancient Stellar System. JWST Proposal. Cycle 1, ID. #2559

Callingham T. M., Cautun M., Deason A. J., Frenk C. S., Grand R. J. J., Marinacci F., 2022, MNRAS, 513, 4107

Campos F. et al., 2016, MNRAS, 456, 3729

Carretta E., Gratton R. G., Bragaglia A., Bonifacio P., Pasquini L., 2004, A&A, 416, 925

Carretta E., Bragaglia A., Gratton R., Lucatello S., 2009, A&A, 505, 139

Cassisi S., Salaris M., 2020, A&AR, 28, 5

Cassisi S., Potekhin A. Y., Pietrinferni A., Catelan M., Salaris M., 2007, ApJ, 661, 1094

Cummings J. D., Kalirai J. S., Tremblay P. E., Ramirez-Ruiz E., Choi J., 2018, ApJ, 866, 21

Davis D. S., Richer H. B., Rich R. M., Reitzel D. R., Kalirai J. S., 2009, ApJ, 705, 398

Di Criscienzo M., Ventura P., D'Antona F., Milone A., Piotto G., 2010, MNRAS, 408, 999

Dotter A. et al., 2010, ApJ, 708, 698

Font A. S., Johnston K. V., Bullock J. S., Robertson B. E., 2006, ApJ, 638, 585

Forbes D. A., Bridges T., 2010, MNRAS, 404, 1203

Gaia Collaboration, 2016, A&A, 595, A1

Gaia Collaboration, 2023, A&A, 674, A1

García-Berro E., Torres S., Althaus L. G., Miller Bertolami M. M., 2014, A&A, 571, A56

Goldsbury R. et al., 2012, ApJ, 760, 78

Gratton R. G., Bragaglia A., Carretta E., Clementini G., Desidera S., Grundahl F., Lucatello S., 2003, A&A, 408, 529

Gratton R. G., Carretta E., Bragaglia A., 2012, A&AR, 20, 50

Griggio M., Nardiello D., Bedin L. R., 2023, Astron. Nachr., 344, e20230006

Hansen B. M. S., 1999, ApJ, 520, 680

Hansen B. M. S. et al., 2002, ApJ, 574, L155

Hansen B. M. S. et al., 2007, ApJ, 671, 380

Hansen B. M. S. et al., 2013, Nature, 500, 51

Harris W. E., 1996, AJ, 112, 1487

Harris W. E., 2010, preprint (arXiv:1012.3224)

Koch A., McWilliam A., 2008, AJ, 135, 1551

Leaman R., VandenBerg D. A., Mendel J. T., 2013, MNRAS, 436, 122

Libralato M. et al., 2018, ApJ, 854, 45

Libralato M. et al., 2022, ApJ, 934, 150

Libralato M. et al., 2023, ApJ, 950, 101

Libralato M. et al., 2024, PASP, 136, 034502

Massari D., Koppelman H. H., Helmi A., 2019, A&A, 630, L4

Massari D. et al., 2023, A&A, 680, A20

Milone A. P., Marino A. F., 2022, Universe, 8, 359

Milone A. P. et al., 2018, MNRAS, 481, 5098

Nardiello D. et al., 2018, MNRAS, 481, 3382

Nardiello D., Bedin L. R., Burgasser A., Salaris M., Cassisi S., Griggio M., Scalco M., 2022, MNRAS, 517, 484

Nardiello D., Griggio M., Bedin L. R., 2023a, MNRAS, 521, L39

Nardiello D., Bedin L. R., Griggio M., Salaris M., Scalco M., Cassisi S., 2023b, MNRAS, 525, 2585

Pietrinferni A. et al., 2021, ApJ, 908, 102

Renedo I., Althaus L. G., Miller Bertolami M. M., Romero A. D., Córsico A. H., Rohrmann R. D., García-Berro E., 2010, ApJ, 717, 183

Richer H., 2009, Is 47 Tuc Young? Measuring its White Dwarf Cooling Age and Completing a Hubble Legacy. HST Proposal ID 11677. Cycle 17

Richer H. B. et al., 2013, ApJ, 778, 104

Rieke M. J. et al., 2023, PASP, 135, 028001

Romero A. D., Campos F., Kepler S. O., 2015, MNRAS, 450, 3708

Salaris M., Cassisi S., Pietrinferni A., 2016, A&A, 590, A64

Salaris M., Cassisi S., Pietrinferni A., Hidalgo S., 2022, MNRAS, 509, 5197

Salaris M., Blouin S., Cassisi S., Bedin L. R., 2024, A&A, 686, A153

Scalco M. et al., 2021, MNRAS, 505, 3549

Scalco M. et al., 2024a, Astron. Nachr., 345, e20240018

Scalco M., Bedin L., Vesperini E., 2024b, A&A, 688, A180

Scalco M. et al., 2024c, A&A, 689, A59

Scalco M. et al., 2025, A&A, 694, A68

Thompson I. B. et al., 2020, MNRAS, 492, 4254

Trujillo-Gomez S., Kruijssen J. M. D., Pfeffer J., Reina-Campos M., Crain R. A., Bastian N., Cabrera-Ziri I., 2023, MNRAS, 526, 5735

VandenBerg D. A., Brogaard K., Leaman R., Casagrande L., 2013, ApJ, 775, 134

Zolotov A., Willman B., Brooks A. M., Governato F., Brook C. B., Hogg D. W., Quinn T., Stinson G., 2009, ApJ, 702, 1058

APPENDIX A: COLOUR–MAGNITUDE DIAGRAMS OF THE WHITE DWARF COOLING SEQUENCE OF 47 TUC

We show in Fig. A1 a set of CMDs of the WD CS of 47 Tuc, using various combinations of the *HST* and *JWST* filters employed in this study. The CMDs include the well-measured sources that passed the PM selection described in Fig. 2.
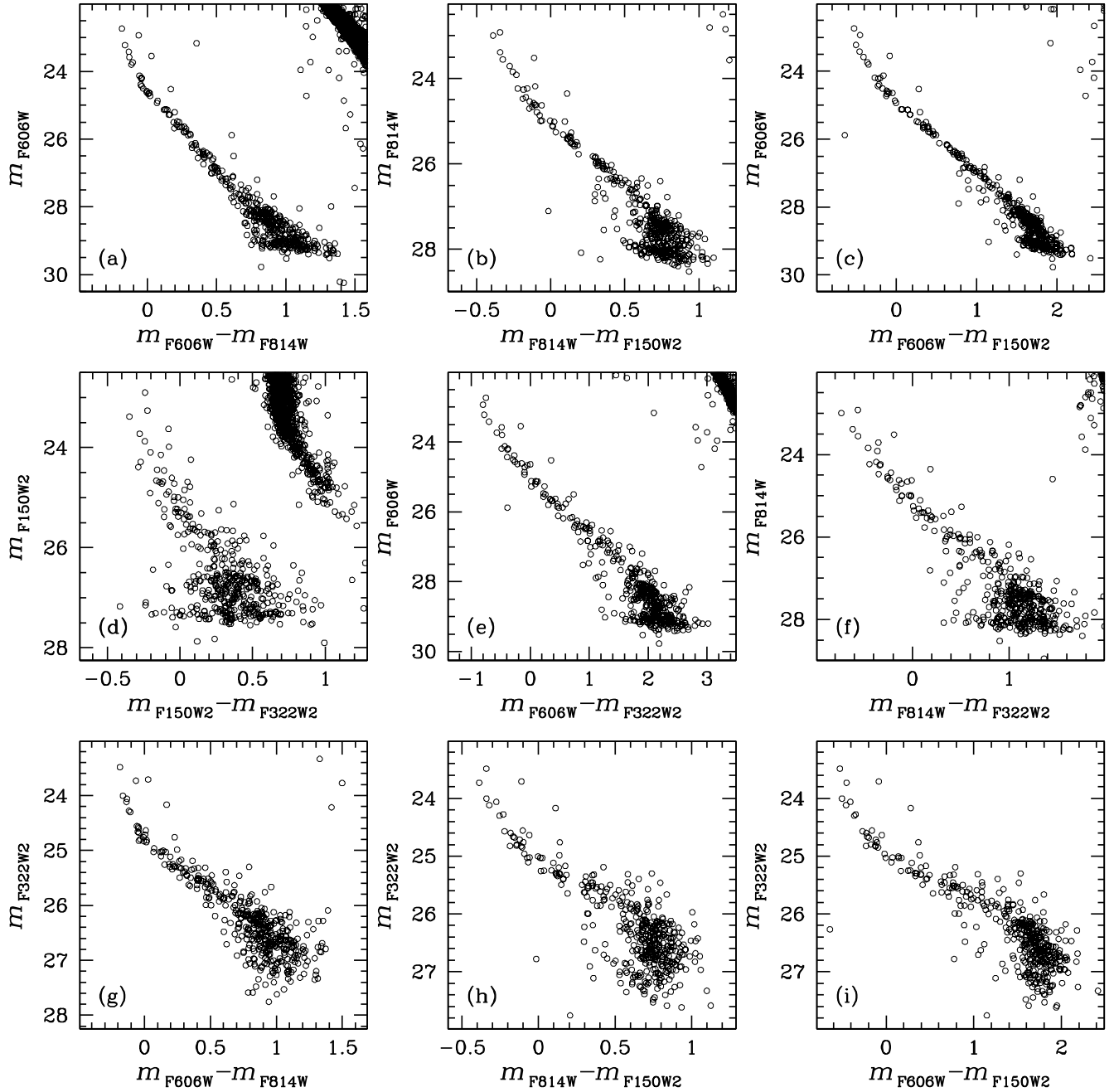
Figure A1. Nine CMDs of 47 Tuc WD CS, using the four *HST* and *JWST* filters employed in this study.

APPENDIX B: LUMINOSITY FUNCTIONS OF THE COOLING SEQUENCE OF 47 TUC

We present in Tables B1 and B2 the LFs of the WD CS from *JWST* and *HST* data, used for the cluster age determination.

Table B1. Completeness-corrected infrared LF of 47 Tuc WDs derived from *JWST* photometry.

m_{F150W2}	N_{stars}	δN_{stars}	m_{F150W2}	N_{stars}	δN_{stars}
22.05	0.00	0.00	24.95	9.93	4.97
22.15	0.00	0.00	25.05	7.78	4.50
22.25	0.00	0.00	25.15	5.43	3.84
22.35	0.00	0.00	25.25	22.81	8.08
22.45	0.00	0.00	25.35	17.92	7.33
22.55	0.00	0.00	25.45	3.14	3.14
22.65	0.00	0.00	25.55	16.51	7.40
22.75	0.00	0.00	25.65	34.85	11.06
22.85	0.00	0.00	25.75	29.52	10.47
22.95	1.56	1.56	25.85	19.54	8.75
23.05	0.00	0.00	25.95	37.36	12.50
23.15	0.00	0.00	26.05	31.00	11.75
23.25	1.65	1.65	26.15	14.23	8.23
23.35	1.67	1.67	26.25	40.88	14.51
23.45	0.00	0.00	26.35	65.83	19.13
23.55	0.00	0.00	26.45	59.21	18.83
23.65	1.73	1.73	26.55	147.91	31.29
23.75	1.75	1.75	26.65	225.19	40.67
23.85	1.78	1.78	26.75	225.33	42.75
23.95	1.82	1.82	26.85	223.33	44.72
24.05	1.86	1.86	26.95	249.66	50.09
24.15	1.90	1.90	27.05	217.72	49.64
24.25	3.88	2.74	27.15	314.15	64.60
24.35	2.00	2.00	27.25	460.62	86.13
24.45	4.13	2.92	27.35	781.79	124.19
24.55	0.00	0.00	27.45	439.15	99.27
24.65	11.03	4.94	27.55	183.82	70.50
24.75	6.86	3.96	27.65	0.00	0.00
24.85	4.76	3.37	27.75	0.00	0.00

Table B2. Completeness-corrected optical LF of 47 Tuc WDs derived from *HST* photometry.

m_{F606W}	N_{stars}	δN_{stars}	m_{F606W}	N_{stars}	δN_{stars}
22.65	0.00	0.00	26.35	11.72	5.88
22.75	1.59	1.59	26.45	23.93	8.52
22.85	0.00	0.00	26.55	12.22	6.13
22.95	1.61	1.61	26.65	3.12	3.13
23.05	0.00	0.00	26.75	6.38	4.52
23.15	0.00	0.00	26.85	22.49	8.56
23.25	1.64	1.64	26.95	16.17	7.27
23.35	0.00	0.00	27.05	9.76	5.65
23.45	1.69	1.69	27.15	19.65	8.07
23.55	3.44	2.44	27.25	6.59	4.67
23.65	0.00	0.00	27.35	10.12	5.86
23.75	3.56	2.52	27.45	17.26	7.76
23.85	0.00	0.00	27.55	7.07	5.01
23.95	0.00	0.00	27.65	21.73	8.93
24.05	0.00	0.00	27.75	29.71	10.59
24.15	5.81	3.36	27.85	31.27	11.15
24.25	1.98	1.98	27.95	12.38	7.17
24.35	2.01	2.01	28.05	52.42	15.32
24.45	2.05	2.05	28.15	74.26	18.88
24.55	6.25	3.62	28.25	108.91	23.77
24.65	8.49	4.25	28.35	76.95	20.19
24.75	2.16	2.16	28.45	138.39	27.92
24.85	2.21	2.21	28.55	71.89	20.23
24.95	2.25	2.25	28.65	115.10	26.33
25.05	0.00	0.00	28.75	77.98	21.96
25.15	9.40	4.71	28.85	78.79	23.10
25.25	7.21	4.17	28.95	195.79	39.13
25.35	0.00	0.00	29.05	299.60	52.16
25.45	5.02	3.56	29.15	329.97	58.65
25.55	5.14	3.64	29.25	211.19	49.33
25.65	15.77	6.47	29.35	134.47	41.70
25.75	5.39	3.81	29.45	14.51	14.56
25.85	13.63	6.12	29.55	35.71	25.45
25.95	0.00	0.00	29.65	0.00	0.00
26.05	0.00	0.00	29.75	33.11	33.40
26.15	11.33	5.68	29.85	0.00	0.00
26.25	2.87	2.87	29.95	0.00	0.00
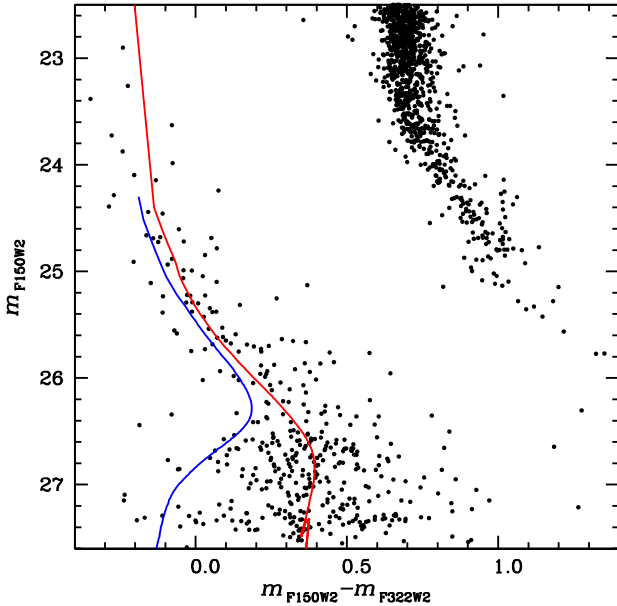
Figure C1. CMD of the 47 Tuc CS and very low MS, together with a 12 Gyr hydrogen-atmosphere WD isochrone (red line – the same used to produce the synthetic WD population shown in Fig. 6) and a 12 Gyr helium-atmosphere WD isochrone (blue line). The isochrones are shifted in magnitude and colour to account for the distance and reddening of the cluster.

APPENDIX C: HELIUM-ATMOSPHERE WDS

Prompted by our referee, we have investigated whether the presence of helium-atmosphere WDs could change the age estimated by considering a pure hydrogen-atmosphere population.

Fig. C1 compares the *JWST* CMD of the cluster CS with the 12 Gyr hydrogen-atmosphere isochrone used to produce the synthetic WD population shown in Fig. 6, and the helium-atmosphere counterpart calculated using the helium-atmosphere BASTI-IAC WD calculations (Salaris et al. 2022). Both isochrones are shifted in magnitude and colour to account for the cluster distance and reddening.

Due to the faster cooling times, the termination of the helium-atmosphere isochrone is located at magnitudes much fainter than the faint limit of our photometry. In the magnitude range of the observed CS, the mass of the objects populating the He-atmosphere isochrone spans a very narrow range, between ~ 0.54 and ~ 0.59 M$_\odot$.

This infrared diagram well separates the two classes of objects at m_{F150W2} fainter than ~ 26.4, where, due to the effect of the different chemical composition on the bolometric corrections to these filters,
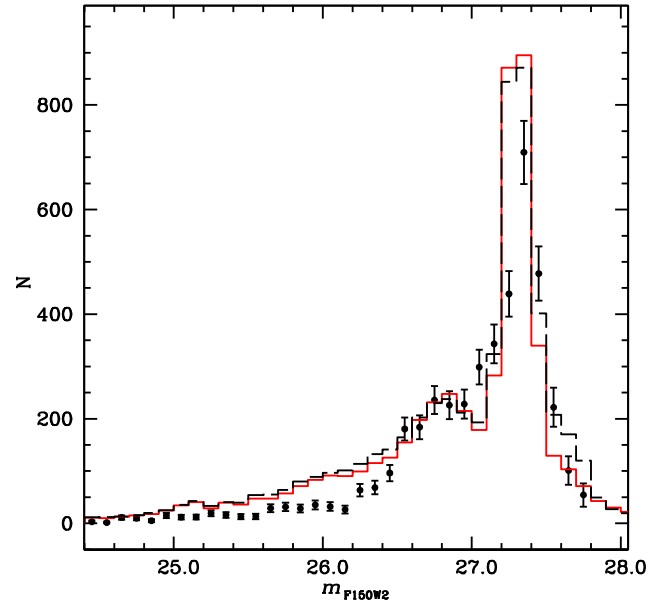
Figure C2. Two 11.5 Gyr WD LFs calculated as described in Section 5, compared to the observed one. The solid red line displays the LF shown in Fig. 7, which considers only hydrogen-atmosphere WD models; the dashed line displays a LF calculated for a population with 75 per cent hydrogen atmosphere, and 25 per cent helium-atmosphere objects, respectively. Both LFs are normalized as described in Section 5.

the helium-atmosphere isochrone lies approximately at the blue end of the observed sequence.

Taken at face value, this comparison seems to confirm that helium-atmosphere objects should make only a small percentage (if any) of the observed cluster WD population.

Nevertheless, we tested the effect of a sizable 25 per cent fraction of helium-atmosphere objects along the observed CS on the theoretical LFs used for our age determination. The result is shown in Fig. C2, which compares the 11.5 Gyr LF that includes only hydrogen-atmosphere WDs, and a counterpart calculated for a population with 75 per cent hydrogen atmosphere and 25 per cent helium-atmosphere objects in the magnitude interval covered by the hydrogen-atmosphere isochrone. Both LFs are normalized as described in Section 5.

The inclusion of the helium-atmosphere objects barely changes the shape of the LF, and the effect on the age determination from the CS is negligible.

This paper has been typeset from a TEX/LATEX file prepared by the author.